Chinese Chemical Letters 35 (2024) 108776

Contents lists available at ScienceDirect

Chinese Chemical Letters

journal homepage: www.elsevier.com/locate/cclet

$Ti_3C_2T_x$ MXene *in-situ* transformed Li_2TiO_3 interface layer enabling 4.5 V-$LiCoO_2$/sulfide all-solid-state lithium batteries with superior rate capability and cyclability

Yaping Wang[a,1], Pengcheng Yuan[a,1], Zeyuan Xu[a], Xiong-Xiong Liu[a], Shengfa Feng[a], Mufan Cao[a], Chen Cao[b], Xiaoqiang Wang[b,*], Long Pan[a,*], Zheng-Ming Sun[a,*]

[a] *Key Laboratory of Advanced Metallic Materials of Jiangsu Province, School of Materials Science and Engineering, Southeast University, Nanjing 211189, China*
[b] *CALB Technology Co., Ltd., Changzhou 213200, China*

ARTICLE INFO

Article history:
Received 22 May 2023
Revised 8 June 2023
Accepted 5 July 2023
Available online 6 July 2023

Keywords:
Solid sulfide electrolyte
Oxide cathode
MXene
In-situ transformation
Li_2TiO_3 interfacial layer

ABSTRACT

All-solid-state lithium batteries (ASSLBs) based on sulfide electrolytes promise next-generation energy storage with high energy density and safety. However, the sulfide electrolytes suffer from phase instability and sluggish interfacial charge transport when pairing with layered oxide cathodes at high voltages. Herein, a simple and efficient strategy is proposed using two-dimensional $Ti_3C_2T_x$ MXene as starting material to *in-situ* construct a 15 nm Li_2TiO_3 layer on a typical oxide cathode, $LiCoO_2$. The *in-situ* transformation of $Ti_3C_2T_x$ into Li_2TiO_3 layer occurs at a low temperature of 500 °C, avoiding the phase deterioration of $LiCoO_2$. The thin Li_2TiO_3 layer is Li^+ conducting and electrochemically stable, thereby preventing the interfacial decomposition of sulfide electrolytes induced by $LiCoO_2$ at high voltages and facilitating Li^+ transport at the interface. Moreover, Li_2TiO_3 can stabilize the layer structure of $LiCoO_2$ at high voltages. Consequently, the sulfide-based ASSLB using $LiCoO_2$@Li_2TiO_3 cathode can operate stably at a high voltage of up to 4.5 V (*vs.* Li^+/Li), delivering an outstanding initial specific discharge capacity of 138.8 mAh/g with a high capacity retention of 86.2% after 100 cycles at 0.2 C. The *in-situ* transformation strategy may also apply to other MXenes, offering a general approach for constructing other advanced lithiated coatings for oxide cathodes.

The rapid growth of electric vehicles provokes the demand for high-energy-density and high-safety electrochemical batteries. However, conventional liquid lithium-ion batteries cannot meet these requirements [1]. In this sense, all-solid-state lithium batteries (ASSLBs) offer a high potential alternative because the liquid electrolytes induced safety concerns can be avoided using the nonflammable solid-state electrolytes [1,2]. Additionally, ASSBLs have higher energy density because they can employ high-voltage cathodes and lithium metal [3,4], and be assembled by internal series-parallel connection [2]. The core component of ASSLBs is the solid-state electrolyte, requiring high ionic conductivity and good contact with electrodes [5,6]. Among various solid-state electrolytes, sulfides show the highest ionic conductivity. For example, the $Li_{10}GeP_2S_{12}$ (LGPS) and $Li_{9.54}Si_{1.74}P_{1.44}S_{11.7}C_{10.3}$ have ionic conductivities of 12 and 25 mS/cm at room temperature, respectively, which are even higher than the commercial liquid electrolytes (~10.7 mS/cm) [6,7]. Moreover, the sulfide electrolytes are naturally soft and have high deformability, which is favorable to forming intimate interfacial contact with electrodes [2,5]. With these advantages, sulfide electrolytes have drawn significant attention in ASSLBs [2,5,8–13].

However, the electrochemical performance of sulfide-based ASSLBs is far from satisfactory, particularly at high voltages [14–17]. First, the sulfide electrolytes have a narrow electrochemical voltage window (1.5-2.1 1 V *vs.* Li^+/Li), indicating that they will undergo interfacial reactions when they contact with oxide cathodes such as $LiCoO_2$ and $LiNi_{1-x-y}Co_xMn_yO_2$ (Scheme 1a), which are usually operated at high voltages (typically ≥ 4.2 V *vs.* Li^+/Li) [9,10,12]. Second, the interfacial reactions are fast and cannot stop until the sulfide electrolytes are completely decomposed, resulting in rapid battery failure (Scheme 1b) [15–19]. Last but not least, the incompatible chemical potentials between the sulfide electrolytes and oxide cathodes will result in the formation of a space charge layer

* Corresponding authors.
E-mail addresses: xiaoqiang.wang@calb-tech.com (X. Wang), panlong@seu.edu.cn (L. Pan), zmsun@seu.edu.cn (Z.-M. Sun).
[1] These authors contributed equally to this work.

https://doi.org/10.1016/j.cclet.2023.108776
1001-8417/

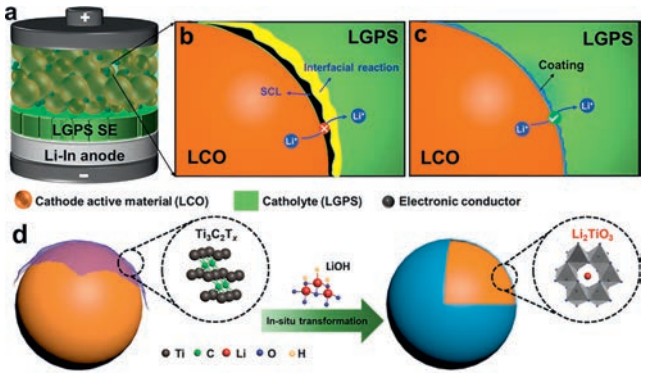

Scheme 1. (a) Configuration of a typical all-solid-state lithium battery based on oxide cathode and sulfide electrolyte. (b) The interfacial issues between oxide cathode and sulfide electrolyte (LCO and LGPS are shown as examples here). (c) The effect that the surface coating layer can impede interfacial reactions and facilitate Li^+ conducting at the cathode/electrolyte interface. (d) The surface coating strategy proposed in this work and the *in-situ* formation of Li_2TiO_3 from 2D $Ti_3C_2T_x$ MXene.

(SCL), further impeding Li^+ transport at the interface (Scheme 1b) [20–23]. Consequently, the sulfide-based ASSLBs show large polarization resistance, low specific capacity, and poor rate and cycling performance [14–17].

To address the interfacial issues between sulfide electrolytes and oxide cathodes, an effective strategy is to construct a surface coating layer on oxide cathodes [17,23–27]. This layer acts as an artificial interphase to prevent the interfacial reactions and relieve SCL effect (Scheme 1c). Generally, lithiated transition metal oxides (LMOs), such as $LiMO_3$ (M = Nb, Ta, V…) [26–29] and Li_2MO_3 (M = Ti, Zr…) [23,25,30], have been extensively investigated as the artificial interphase, as they show relatively high ionic conductivity (10^{-5}-10^{-7} S/cm) that can diminish the SCL polarization by mitigating the potential drop between sulfide electrolytes and oxide cathodes [21,23,24]. Additionally, LMOs are chemically/electrochemically stable against sulfide electrolytes and oxide cathodes [31–33]. Generally, metal-organic compounds are used as starting materials, *e.g.*, tetrabutyl titanate or titanium tetraisopropoxide, which require high-temperature annealing (usually at 800 °C) to form LMO layers [23,34]. However, high-temperature annealing usually deteriorates the phase structures of oxide cathodes, resulting in poor electrochemical performance [35,36]. Therefore, it is of great importance to develop a general and effective strategy to construct ultrathin and uniform LMO coating at lower annealing temperatures.

MXenes, *i.e.*, transition metal carbide/nitrides, are a new member of the two-dimensional (2D) nanomaterial family [37]. The general chemical formula of MXenes can be written as $M_nX_{n+1}T_x$, where M is the early transition metals, X is carbon and/or nitrogen, and T is the surface functional groups such as −F and –OH [37–39]. In addition to the diverse compositions, MXenes can also be easily oxidized into transition metal oxides at mild conditions, because the transition metals of MXenes are in low valence states and have high reducibility [38,39]. These merits make MXenes an ideal starting material to construct LMO layers on oxide cathodes at low temperatures. Moreover, the ultrathin nature and good dispersion of MXene can guarantee the formation of thin and uniform LMO coating layer on oxide cathodes [37–40].

Herein, in this contribution, a typical $Ti_3C_2T_x$ MXene is proposed as the starting material to *in-situ* construct an ultrathin and homogeneous Li_2TiO_3 (LT) layer on the surface of the $LiCoO_2$ (LCO) cathode, labeled as LCO@LT. The transformation of $Ti_3C_2T_X$ MXene into Li_2TiO_3 occurs at a low temperature of only 500 °C, thereby avoiding the high-temperature-induced phase deterioration of LCO. The uniform and electrochemically stable Li_2TiO_3 layer can isolate the LCO from sulfide electrolytes (*viz.* LGPS in this work), which can prevent the interfacial decomposition of LGPS. The Li_2TiO_3 layer can also stabilize the LCO cathode at high voltages. Furthermore, the Li_2TiO_3 layer is Li^+ conducting, which can facilitate Li^+ transport at the interface and relieve the SCL effect between LCO and LGPS. Consequently, the ASSLBs using LCO@LT cathode and LGPS solid-state electrolyte can be operated at a high cutoff voltage of 4.5 V *vs.* Li^+/Li, exhibiting a high specific capacity of 105 mAh/g at a high rate of 0.5 C, significantly higher than that (58.9 mAh/g) of bare LCO cathode-based ASSLBs. Additionally, the ASSLB with LCO@LT cathode shows a capacity retention of 86.2% after 100 cycles at 0.2 C, while the bare LCO cathode merely delivers 9.2%.

The synthesis process of LCO@LT cathode using $Ti_3C_2T_x$ nanosheet as starting material been displayed in Scheme 1d. In the first step, $Ti_3C_2T_x$ nanosheets were self-assembled on the surface of the LCO particles. Typically, 1 g LCO (Macklin, 99.8%) was dispersed in 100 mL 1 wt% poly(diallyl dimethylammonium chloride) (PDDA, 20 wt% in water, Sigma-Aldrich) solution and the excessive PDDA was removed by washing the mixture with deionized water through centrifugation. The crystalline structure and microstructure of $Ti_3C_2T_x$ nanosheets and LCO@$Ti_3C_2T_x$ powder are shown in Fig. S1 (Supporting information). Then, the PDDA-modified LCO particles were dispersed again in deionized water by ultrasonic dispersion and magnetic stirring to form a homogeneous suspension. At the same time, 15 mL $Ti_3C_2T_x$ dispersion with a concentration of 1 mg/mL was dripped into the as-prepared PDDA-modified LCO suspension, and then 100 mg LiOH (Macklin, 98%) was added. Secondly, the resulting suspension was dried at 80 °C for 24 h in a vacuum oven to remove the water and get dry LCO@$Ti_3C_2T_x$ powders. Finally, the LCO@$Ti_3C_2T_x$ powders were annealed at 400-800 °C for 4 h in air. Note that the $Ti_3C_2T_x$ nanosheets in this work were derived by HCl/LiF etching Ti_3AlC_2 and the detailed preparation process can be referred in our previous work [38].

The electrochemical properties of the cathodes were evaluated based on the ASSLB configurations. LPGS (99%, HF-Kejing) and vapor-grown carbon fiber (VGCF, Showa Denko) was used as the solid electrolyte and electron conductor of the composite cathode (CC), respectively. The bare LCO and LCO@LT were employed as cathode materials of the ASSLB for comparison. Firstly, the cathode material and LGPS were mixed by hand ground in an Ar-filled glove box (mBraun, MB-10-G-V2A) at a weight ratio of 68:30 and then an additional 2 wt% VGCF was added and continuously mixed to get a uniform CC powder. Secondly, a homemade poly(ether ether ketone) (PEEK) cylinder and two steel stamps with diameters of 10 mm were prepared (Fig. S2 in Supporting information). 60 mg LGPS powder was added into the PEEK cylinder and pressed at 300 MPa for 5 min as the solid electrolyte pellet. Then, 8 mg CC powders (corresponding to a an active material mass loading of ~6.93 mg/cm^2) were added to one side of the LGPS pellet and pressed at 380 MPa. Finally, a 120 μm thick Li foil (Φ = 6 mm, 99.99%) and 125 μm thick In foil (Φ = 9 mm, 99.999%) were placed at the other side with In foil closing to the LGPS electrolyte pellet and then pressed at 120 MPa to form a whole ASSLB. To ensure the gas sealing of the full cells during testing, two silicon gaskets were placed on both sides of the PEEK cylinder (Fig. S1).

All the battery tests were conducted at 40 °C controlled by a thermostat (Lichen 202-00T, Shanghai). The galvanostatic charge/discharge tests were conducted on Neware CT-4008 tester at a voltage range of 2.00-3.88 V (*vs.* Li^+/Li-In), which corresponds to 2.62-4.50 V (*vs.* Li^+/Li) at current densities of 0.05, 0.1, 0.2, 0.5 and 1 C, respectively (1 C = 150 mAh/g) [30,41]. The cycling performances of the batteries were evaluated at 0.2C after first tested at 0.05 C for three cycles. EIS curves of the ASSLBs before and after cycling were tested on Biologic VSP1 electrochemical workstation at 10 mV with a frequency ranging from 0.01 Hz to 500 kHz.

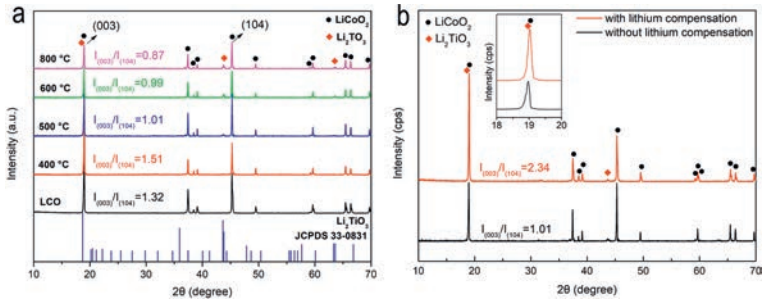

Fig. 1. XRD patterns of (a) LCO and the LCO@$Ti_3C_2T_x$ annealed at 400–800 °C and (b) LCO@$Ti_3C_2T_x$ annealed at 500 °C with and without lithium compensation.

XRD patterns were recorded by Haoyuan DX-2700BH X-ray diffractor with Cu-Kα radiation ($\lambda = 1.5418$) over the range of 10°−70°. To isolate the LGPS-based cathode from the air, a thin mylar film (Premierlabsupply, TF-115) was put on the surface of LGPS-based cathode and sealed in a glove box for XRD tests. SEM images were acquired by an FEI Sirion 200 field emission scanning electron microscope (FESEM) equipped with Oxford Aztec X-MAX 80 energy disperse spectroscopy (EDS). The particle size was estimated by image analysis using the Image Profession Plus 6.0 software. TEM images were obtained on a ThermoFisher Talos F200X high-resolution transmission electron microscope (HRTEM) that was equipped with an EDS for element mapping analysis. The particle size distribution of the LCO powders before and after surface coating was analyzed by image analysis using an Image Profession Plus software.

The annealing conditions were carefully regulated to achieve a well-crystallized LCO@LT cathode material. Fig. 1a shows the XRD patterns of the LCO@$Ti_3C_2T_x$ annealed at increasing temperatures from 400 °C to 800 °C. No obvious phase change is detected below 500 °C, but some minor peaks (♦) corresponding to the Li_2TiO_3 phase (JCPDS No. 33–0831) are detected at 500 °C. This result indicates that $Ti_3C_2T_x$ has been chemically converted to Li_2TiO_3 at 500 °C. With temperature increases, the Li_2TiO_3 peaks become more detectable, but the peak intensity ratio of (003) and (104) planes ($I_{(003)}/I_{(104)}$) of the LCO phase obviously decreases, implying a reduction in the structural ordering of the LCO bulk phase [42,43]. Therefore, to form the Li_2TiO_3 coating phase and maintain the bulk phase of LCO, a relatively low annealing temperature of 500 °C was adopted. Fig. 1b shows the XRD patterns of LCO@$Ti_3C_2T_x$ annealed at 500 °C with and without lithium compensation. When additional lithium was compensated, the $I_{(003)}/I_{(104)}$ value increases from 1.01 to 2.34, indicating a lower cation mixing and better layered structure of LCO [42,44]. This is because the additional lithium compensates for the lithium volatilization during heat treatment and thus impedes the structural distortion of the LCO cathode.

Figs. 2a-f show the SEM images and corresponding particle size distribution of the bare LCO and LCO@LT powders. The bare LCO particles exhibit a smooth surface and the particle sizes distribute at 1–18 μm with an average size of 7.4 μm. After surface coating, LCO@LT particles show a relatively coarse surface, and the particle sizes distribute at 2–18 μm with an average value of 8.2 μm, slightly larger than the bare LCO. This maybe comes from the dual effect of surface coating and agglomeration of several small LCO particles wrapped by $Ti_3C_2T_x$ nanosheets during the surface coating process. The chemical element ratio of LCO@LT is evaluated by energy dispersive spectrometer (EDS) analysis and the results are shown in Fig. S3 (Supporting information). Accordingly, the weight ratio of Li_2TiO_3 coating to LCO bulk is calculated to be ~1.2 wt%.

To get more detailed information about the surface component and morphology of LCO@LT, high-resolution TEM was performed and the results are shown in Figs. 2g-i. A relatively uniform coating layer is observed on the micron-sized LCO@LT particle (~5 μm). At the surface edge of LCO@LT particles, a clear lattice fringe with interlayer distance of 0.22 nm is observed, which can be indexed as ($\bar{1}33$) plane of the Li_2TiO_3 phase [35,36]. This is consistent with the XRD analysis of LCO@LT in Fig. 1. The element mappings in Fig 2i also verify the formation of Li_2TiO_3 coating layer on the surface of LCO particle, in which Ti and O elements are visibly enriched with a thickness of ~15 nm.

The influence of Li_2TiO_3 surface coating on the electrochemical properties of LCO cathode has been investigated based on ASSLB using LGPS as the electrolyte in a voltage range of 2.00–3.88 V *vs.* Li^+/Li-In (corresponding to 2.62–4.50 V *vs.* Li^+/Li) at 40 °C [23,30,34]. Fig. 3a shows the rate performance of the ASSLB with bare LCO and LCO@LT cathodes. The specific discharge capacities of LCO@LT cathode at low C-rates are slightly higher than LCO, for example, the average specific discharge capacities of LCO and LCO@LT cathodes at 0.2 C are 127.3 mAh/g and 137.1 mAh/g, respectively. However, with increasing C-rate, the specific discharge capacities of LCO cathode at 0.5 C and 1 C quickly degrade to 58.9 mAh/g and 24.5 mAh/g, respectively. In contrast, the LCO@LT cathode remains 105 mAh/g and 72.5 mAh/g at 0.5 C and 1 C, respectively. The rapid degradation of bare LCO cathode, especially at high C-rates, mainly comes from the large polarization resistance resulting from the severe interfacial reactions between LCO and LGPS. As for LCO@LT cathode, the Li_2TiO_3 layer acts as an interfacial layer that protects the LGPS electrolyte from decomposition and reserves the pathways for Li^+ transport, leading to decreased cathodic polarizations and improved rate capabilities of the LCO@LT cathode.

To gain further insight into the reaction kinetics, Fig. S4 (Supporting information) showcases the detailed charge/discharge curves and corresponding differential capacity plots of the ASSLBs with LCO and LCO@LT cathodes respectively, at different C-rates. The overpotentials and the voltage drops (Figs. S4a and b) of the LCO@LT cathode are lower than those of the LCO cathode, especially at high C-rates. These results can be referred to the decreased polarization resistance of the ASSLB with LCO@LT cathode instead of LCO cathode [28,30,41]. As physical issues such as cracks and contact loss have not significantly emerged during C-rate tests for both cathodes, the polarization decrement of the LCO@LT cathode mainly comes from the accelerated kinetics [41]. Besides, the voltage gap between the redox peaks (ΔE_{redox}) of the LCO@LT cathode at 1 C is lower (0.47 V) than that of LCO cathode (0.53 V) (Figs. S4c and d), indicating that the LCO@LT cathode exhibits improved lithium intercalation/deintercalation kinetics due to the stabilized interfaces between LCO and LGPS [27,28,41].

Fig. 3b shows the cycling performance of the ASSLB with bare LCO and LCO@LT cathodes at 0.2 C. For the LCO cathode, the specific discharge capacity shows a sharp degradation after 20 cycles and only retains 9.2% after 100 cycles. In comparison, the LCO@LT cathode presents a high initial specific discharge capacity of 138.8 mAh/g and stable cycling with a capacity retention of 86.2% after 100 cycles. The average capacity decay of LCO@LT cathode is 0.16

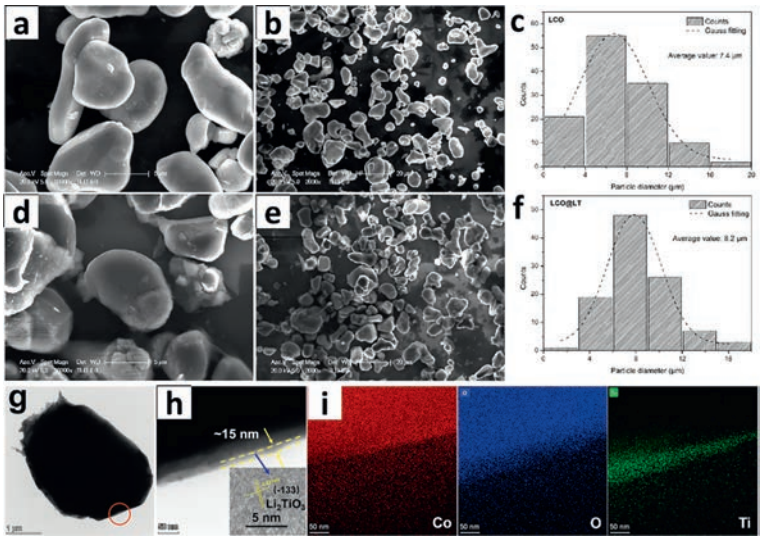

Fig. 2. SEM images and corresponding particle size distribution of (a-c) the bare LCO and (d-f) the LCO@LT. HRTEM images of (g) LCO@LT particle and (h) the surface region as marked in the red circle in (g) and the corresponding EDS mapping of Co, O, Ti. The yellow dash in (h) refers to the surface coating, and the inset is the lattice fringe image of the coating material.

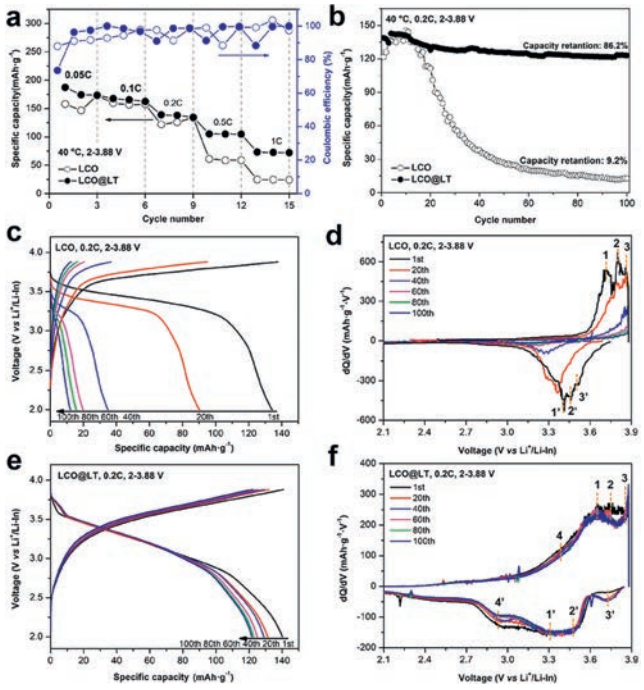

Fig. 3. (a) Rate and (b) cycling performance of the ASSLB with bare LCO and LCO@LT cathodes. The charge/discharge curves and corresponding differential capacity plots of the ASSLB with (c, d) LCO cathode and (e, f) LCO@LT cathode at different cycle numbers at 0.2 C at 40 °C.

mAh/g per cycle, showing great improvement than bare LCO cathode. Figs. 3c-f show the charge/discharge curves and corresponding differential capacity plots of the ASSLBs with LCO and LCO@LT cathodes at different cycles. With increasing cycle tests, the LCO cathode shows obvious shrinkage in peak areas and gradual broadening in voltage gap between the redox peaks, which are indicative of severe structural degradation and capacity loss induced by continuous interfacial reactions resulting in tougher lithium intercalation/deintercalation reactions in LCO cathode [45]. As for the LCO@LT cathode, the capacity differential plots are slightly varied. These phenomena indicate that the interfacial side reactions are basically impeded during the long-term cycling and thus lead to the improved high voltage cyclability of the LCO@LT cathode.

With further observation of the involved reactions, three pairs of redox peaks have been observed for both cathodes, in which peaks 1 and 1' correspond to the coexistence of two distinct hexagonal phases, and the peak pairs at higher voltages (peaks 2 and 2', peaks 3 and 3') corresponding to the phase transition between ordered and disordered lithium ion arrangements in the CoO_2 framework [15,46]. Besides, an additional but minor redox peaks pair (peaks 4 and 4') at lower voltages is observed for the LCO@LT cathode, which can be attributed to the formation of the LT-$LiCoO_2$ phase during the annealing process at 500 °C [46,47]. With increasing cycle tests, the peak 1' shifts to lower voltage and the peak intensity decrease obviously, and the redox peaks at higher voltages (peaks 2 and 2', peaks 3 and 3') become invisible in LCO after being tested for 20 cycles but keep remained in LCO@LT cathode. The decrease of peak 1' and the disappearing of redox peaks at higher voltage can be associated with the crystalline structure or surface component decay of the LCO cathode induced by high-voltage cycling [41,46,47]. In comparison, the improved cyclability of LCO@LT cathode can be attributed to the surface coating of Li_2TiO_3 which can help to maintain the layered phase structure of LCO cathode at high voltages, and this has been verified by phase structure and microstructure analysis of the cycled cathode in the following text in below.

Figs. 4a and b show the Nyquist plots and corresponding fitting curves of the ASSLB with bare LCO and LCO@LT cathode after the 3rd and 100th cycling test at 0.2 C. The Nyquist plots are characterized with an asymmetric semi-circle at the high frequency and a straight line at the low frequency at the beginning. After 100 cycle tests, the high-frequency curves evolve to two distinct semi-circles. The results indicate three reaction processes are involved [15]. Therefore, a typical equivalent circuit consisting of $R_{ohm}(R_1Q_1)(R_2Q_2)W$ (Fig. S5 in Supporting information) is selected for impedance fitting and the fitting parameters are listed in Table S1 (Supporting information). R_{ohm}, R_1, and R_2 refer to the polarization resistances originating from the bulk diffusion of Li^+ and electrons, interfacial Li^+ diffusion, and the charge transfer processes, respectively [15]. The sum of R_1 and R_2 is denoted as overall polarization resistance (R_p).

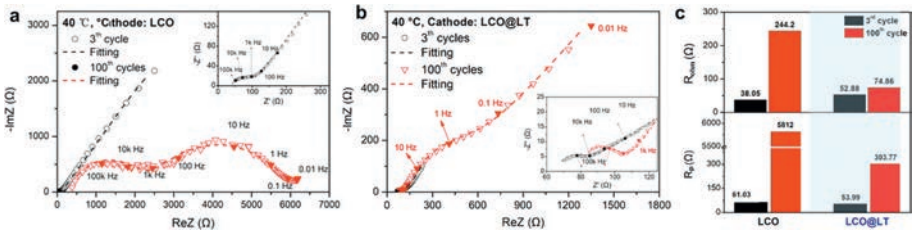

Fig. 4. The Nyquist plots and corresponding fitting curves of the ASSLB with (a) LCO and (b) LCO@LT cathode after the 3rd and 100th cycling test at 0.2 C. (c) The variation of the R_{ohm} and R_p values derived from impedance fitting after the 3rd and 100th cycle for ASSLB with LCO and LCO@LT cathodes.

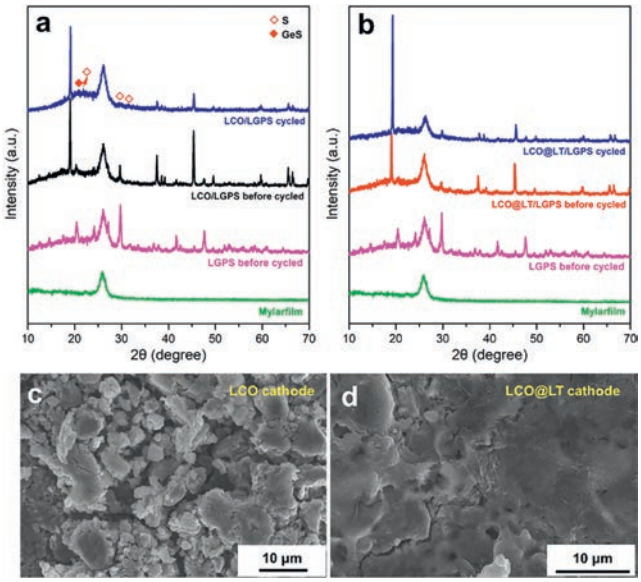

Fig. 5. XRD patterns of (a) LCO and (b) LCO@LT cathodes with LGPS as electrolytes before and after the 100 cycling tests at 0.2 C. The top-view SEM images of the (c) LCO and (d) LCO@LT cathodes with LGPS as electrolytes after the 100 cycle tests at 0.2 C.

Fig. 4c shows the R_{ohm} and R_p values derived from impedance fitting after the 3rd and 100th cycle for ASSLB with bare LCO and LCO@LT cathode. Note that the anode side of the full cells has been kept the same, the changes in impedance resistance can mostly be owed to the cathode side [15,27,41]. R_{ohm} soars from 38.05 Ω to 244.2 Ω for LCO, while slightly varies from 52.88 Ω to 74.86 Ω for LCO@LT. The quick increase of R_{ohm} for LCO mainly comes from LGPS decomposition and contact loss within the battery [15]. The slightly varied R_{ohm} for LCO@LT indicates that the decomposition of LGPS electrolyte and the physical contact loss can be suppressed by surface coating, which has been validated by the postmortem XRD and SEM analysis of the cycled cathode in the below (Fig. 5). Moreover, the R_p value for LCO increased by nearly 93 times, while LCO@LT increased by only 5 times. This phenomenon further validates that the suppressed interfacial reaction and stabilized interface are helpful to interfacial Li^+ diffusion and charge transfer processes within the LCO@LT cathode.

To better elucidate the phase and structure evolution during high voltage cycling, postmortem analysis of the component phase and morphology of the cycled cathode were conducted. Figs. 5a and b show the XRD patterns of LCO and LCO@LT cathodes with LGPS as electrolytes before and after 100 cycles at 0.2 C, respectively. For the LCO@LT cathode, no discernable structural change is detected after 100 cycles, whereas new phases assigned to S and GeS are found for the LCO cathode, and the peaks corresponding to LGPS are greatly weakened and nearly invisible. The new phases (GeS, S) are the by-products of LGPS decomposition induced by LCO at high voltage with strong oxidation ability. Furthermore, due to the electronic conducting nature of the by-products [48], the decomposition of LGPS would be continued, and thus the bulk resistance and polarization resistance show a quick increase for LCO cathode (Fig. 4c). Benefiting from the Li_2TiO_3 interlayer which is Li^+-conducting and electronic insulating, the LGPS electrolyte is separated from the high voltage cathode and the decomposition reactions are efficiently impeded. Figs. 5c and d show the top-view SEM images of the cathodes after 100 cycles at 0.2 C. As shown, great cracks and particle pulverization are observed for cycled LCO cathode, while LCO@LT presented a relatively integrated structure except for some minor pores and cracks. The result further verifies that the Li_2TiO_3 interlayer plays an important role in protecting the LGPS electrolyte from interfacial decomposition and stabilizing the LCO/LGPS interface during high-voltage cycling.

In summary, a novel and efficient surface coating technique was proposed to synthesize Li_2TiO_3 using a 2D $Ti_3C_2T_x$ nanosheet as the starting material. Due to the high chemical-reactivity of $Ti_3C_2T_x$ nanosheet at oxidation atmosphere, the annealing temperature to form Li_2TiO_3 coating is much lower (500 °C) than the reported solvent-based method (800 °C), avoiding the structural decay of LCO cathode induced by high-temperature annealing. The polarization resistances of the ASSLBs with LCO@LT cathode are greatly diminished for the improved interfacial stability between $LiCoO_2$ and LGPS by Li_2TiO_3 interphase. Moreover, the layer structure of the LCO cathode at high voltages can also be stabilized by the Li_2TiO_3 layer. As a result, the ASSLB with LCO@LT cathode shows a specific discharge capacity of 105 mAh/g at 0.5 C, higher than that of 58.9 mAh/g with bare LCO cathode. At the same time, the ASSLB with LCO@LT cathode shows a more stable cyclability with a capacity retention of 86.2% after 100 cycles at 0.2 C with a high cutoff voltage up of 4.5 V *vs.* Li^+/Li. Generally, this work provides a novel and viable way to optimize the performance of ASSLB based on high-voltage oxide cathode and sulfide electrolyte.

Declaration of competing interest

The authors declare that they have no known competing financial interests or personal relationships that could have appeared to influence the work reported in this paper.

Acknowledgments

The authors acknowledge the financial support from the National Natural Science Foundation of China (Nos. 52201242, 52250010), Natural Science Foundation of Jiangsu Province (Nos. BK20200386, BK20200186), Young Elite Scientists Sponsorship Program by CAST (No. 2021QNRC001), and the Fundamental Research Funds for the Central Universities (No. 2242022R40018). The authors thank Zhihua Tian and Lingqiao Kong for acquiring SEM and TEM images.

Supplementary materials

Supplementary material associated with this article can be found, in the online version, at doi:10.1016/j.cclet.2023.108776.

References

[1] R. Chen, Q. Li, X. Yu, et al., Chem. Rev. 120 (2020) 6820–6877.
[2] L. Liu, J. Xu, S. Wang, et al., Etransportation 1 (2019) 100010.
[3] X. Fan, M. Liu, R. Zhang, et al., Chin. Chem. Lett. 33 (2022) 4421–4427.
[4] J. Liu, H. Yuan, H. Liu, et al., Adv. Energy Mater. 12 (2022) 2100748.
[5] J. Lau, R.H. DeBlock, D.M. Butts, et al., Adv. Energy Mater. 8 (2018) 1800933.
[6] Y. Kato, S. Hori, T. Saito, et al., Nat. Energy 1 (2016) 16030–16036.
[7] N. Kamaya, K. Homma, Y. Yamakawa, et al., Nat. Mater. 10 (2011) 682–686.
[8] J. Wu, L. Shen, Z. Zhang, et al., Electrochem. Energy Rev. 4 (2021) 101–135.
[9] Z. Jiang, S. Chen, C. Wei, et al., Chin. Chem. Lett. 35 (2024) 108561.
[10] G. Peng, X. Yao, H. Wan, et al., J. Power Sources 307 (2016) 724–730.
[11] S. Yang, B. Wang, Q. Lv, et al., Chin. Chem. Lett. 34 (2023) 107783.
[12] J. Yin, X. Yao, G. Peng, et al., Solid State Ion. 274 (2015) 8–11.
[13] Y. Jin, Q. He, G. Liu, et al., Adv. Mater. 35 (2023) 2211047.
[14] C. Chen, M. Jiang, T. Zhou, et al., Adv. Energy Mater. 11 (2021) 2003939.
[15] W. Zhang, F.H. Richter, S.P. Culver, et al., ACS Appl. Mater. Interfaces 10 (2018) 22226.
[16] K. Takada, N. Ohta, L. Zhang, et al., Solid State Ion. 225 (2012) 594–597.
[17] Y. Li, D. Zhang, X. Xu, et al., J. Energy Chem. 60 (2021) 32–60.
[18] A. Banerjee, H. Tang, X. Wang, et al., ACS Appl. Mater. Interfaces 11 (2019) 43138–43145.
[19] Y. Liao, J. Hu, Z. Fu, et al., J. Energy Chem. 80 (2023) 458–465.
[20] L. Wang, R. Xie, B. Chen, et al., Nat. Commun. 11 (2020) 5889–5897.
[21] J. Liang, X. Zeng, X. Zhang, et al., J. Am. Chem. Soc. 140 (2018) 6767–6770.
[22] W. He, L. Zhou, M.K. Tufail, et al., Trans. Tianjin Univ. 27 (2021) 423–433.
[23] N. Ohta, K. Takada, L. Zhang, et al., Adv. Mater. 18 (2006) 2226–2229.
[24] U. Nisar, N. Muralidharan, R. Essehli, et al., Energy Storage Mater. 38 (2021) 309–328.
[25] J.W. Lee, Y.J. Park, J. Electrochem. Sci. Technol. 9 (2018) 176–183.
[26] N. Ohta, K. Takada, I. Sakaguchi, et al., Electrochem. Commun. 9 (2007) 1486–1490.
[27] X. Li, L. Jin, D. Song, et al., J. Energy Chem. 40 (2020) 39–45.
[28] J. Shi, Z. Ma, K. Han, et al., J. Mater. Chem. A 10 (2022) 21336.
[29] A. Müller, F. Okur, A. Aribia, et al., Mater. Adv. 4 (2023) 2138–2146.
[30] C. Wang, F. Ren, Y. Zhou, et al., Energy Environ. Sci. 14 (2021) 437–450.
[31] Y. Xiao, L.J. Miara, Y. Wang, et al., Joule 3 (2019) 1252–1275.
[32] Y. Zhu, X. He, Y. Mo, J. Mater. Chem. A 4 (2016) 3253–3266.
[33] A.M. Nolan, Y. Liu, Y. Mo, Acs Energy Lett. 4 (2019) 2444–2451.
[34] Z. Li, Z. Wang, Y. Miao, et al., J. Power Sources 541 (2022) 231703.
[35] J. Liu, Z. Wu, M. Yu, et al., Small 18 (2022) 2106337.
[36] J. Cao, H. Xie, F. Lv, et al., Acs Appl. Energy Mater. 3 (2020) 5462–5471.
[37] X. Li, Z. Huang, C.E. Shuck, et al., Nat. Rev. Chem. 6 (2022) 389–404.
[38] H. Zhang, L. Yang, P. Zhang, et al., Adv. Mater. 33 (2021) 2008447.
[39] D. Sha, C. Lu, W. He, et al., ACS Nano 16 (2022) 2711–2720.
[40] M. Xia, B. Chen, F. Gu, et al., ACS Nano 14 (2020) 5111–5120.
[41] R.S. Negi, P. Minnmann, R. Pan, et al., Chem. Mat. 33 (2021) 6713–6723.
[42] J. Fu, Y. Bai, C. Liu, et al., Mater. Chem. Phys. 115 (2009) 105–109.
[43] L. Cao, H. Wang, Z. Guo, et al., J. Mater. Chem. A 11 (2023) 9913–9921.
[44] H. Nie, L. Xu, D. Song, et al., Green Chem. 17 (2015) 1276–1280.
[45] J. Zhang, C. Liu, H. Zhang, et al., J. Mater. Chem. A 11 (2023) 8766–8775.
[46] W. Yoon, K. Kim, J. Power Sources (1999) 517–523.
[47] K. Dokko, S. Horikoshi, T. Itoh, et al., J. Power Sources 90 (2000) 109–115.
[48] M. Nakamura, E.G. Víllora, T. Ohsawa, et al., J. Cryst. Growth 609 (2023) 127153.